A Robotic Strategy for In-Plane Center of Rotation Identification and Control in Atomic Force Microscopy

Freddy Romero Leiro, Stéphane Régnier, Sinan Haliyo, Mokrane Boudaoud

A Robotic Strategy for In-Plane Center of Rotation Identification and Control in Atomic Force Microscopy

Freddy Romero Leiro, Stéphane Régnier, Sinan Haliyo, and Mokrane Boudaoud

***Abstract*—This letter presents a method to determine and control the center of rotation of a parallel micro-robotic platform used as a sample holder for an Atomic Force Microscope (AFM). The AFM is operating inside a Scanning Electron Microscope (SEM) for correlative AFM in SEM imaging. The objective is to spatially co-localize the Pivot Point (PP) and the AFM tip at any region of interest of a sample within the reachable workspace of the AFM. To do so, SEM images are used to land the AFM tip on a desired Point Of Interest (POI). Topographic data obtained with the AFM are used to calculate the Tool Center Point (TCP) of the robot and to identify the coordinates of the POI in the AFM sample holder reference frame. The position of the PP is then controlled relying on the TCP and SEM vision to finally been able to perform, in a controlled way, in-plane rotations of the sample holder around the AFM tip with a micrometer precision. This work shows for the first time how SEM and AFM data can be used in tandem to calibrate the rotational degrees of freedom of an AFM system.**

***Index Terms*—Automation at Micro-Nano Scales, Calibration and Identification, Parallel Robots, Kinematics.**

I. INTRODUCTION

THE Atomic Force Microscope (AFM) allows manipulation [1], topography imaging [2], force measurement [3] and analysis of dynamic processes at the very small scales [4]. AFM systems are often used in combination with other microscopy technologies to perform correlative microscopy, including light microscopy (LM) and/or scanning electron microscopy (SEM). In the case of correlative AFM/SEM, it can be performed either in situ with an AFM inside the SEM (AFM in SEM), or with a separate equipment whose images are correlated during post-processing. Currently available solutions for AFM in SEM improve the user's workflow compared to separate AFM/SEM solutions on compatible samples [5]–[8]. All correlative AFM in SEM solutions proposed in the literature use Cartesian AFM scanners which strongly limit the degrees of freedom of the AFM probe relatively to the sample. This restriction does not allow for example to rotate the sample on the AFM scan plane to favor specific scan trajectories but also to control the orientation of the probe to solve accessibility issues [9], [10].

Manuscript received: June 15, 2023; Revised: September 20, 2023; Accepted: October 20, 2023.

This paper was recommended for publication by Editor Xinyu Liu upon evaluation of the Associate Editor and Reviewers' comments.

F. Romero Leiro, S. Régnier, S. Haliyo and M. Boudaoud, are with Sorbonne Université, Institut des Systèmes Intelligents et de Robotique, UMR 7222, ISIR, F-75005 Paris, France. Emails: romeroleiro@isir.upmc.fr, stephane.regnier@sorbonne-universite.fr, sinan.haliyo@sorbonne-universite.fr, mokrane.boudaoud@sorbonne-universite.fr.

Digital Object Identifier (DOI): see top of this page.

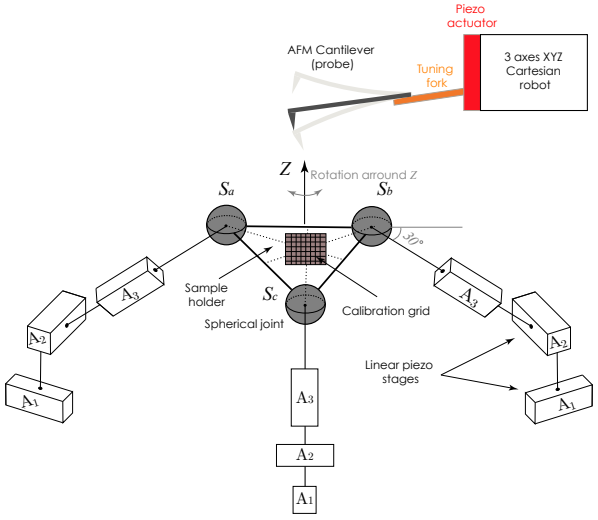

Fig. 1: Micro-robotic system consisting of a PPPS parallel platform and a 3-DOF Cartesian AFM scanner.

It is not straightforward to design rotation joints that allow both in-plane and out-of-plane micro-scale motions. To design a micro-robotic system with rotations capabilities in the three-dimensional space, compliant mechanisms can be integrated [11] but the use of spherical joints [12] is one of the best solutions up to now. Out-of-plane rotational DOFs can be used to calibrate the orientation of the sample plane so that the AFM probe can make a force measurement along the axis normal to this plane [13], [14]. For this purpose, it is possible to include specific patterns inscribed in the sample holder [13] or to perform an AFM scan on a free surface of the sample substrate to calculate the scan plane [14].

A critical aspect when using robotic structures with rotating DOFs for AFM in SEM is to keep the center of rotation within the field of view of the SEM [15] and close to the AFM tip. Depending on the task resolution and SEM magnification, this requirement can become very complex and difficult to meet, i.e., the higher the SEM magnification, the more difficult it is to accurately identify the center of rotation and keep it in the field of view. In addition, the coordinates of the center of rotation are affected by several sources of error, mainly the elastic deformations of the robotic links and the clearances in the joints. Clearances in the joints exists in all types of robotic structures that allow rotation in three-

This article has been accepted for publication in IEEE Robotics and Automation Letters. This is the author's version which has not been fully edited and content may change prior to final publication. Citation information: DOI 10.1109/LRA.2023.3333684

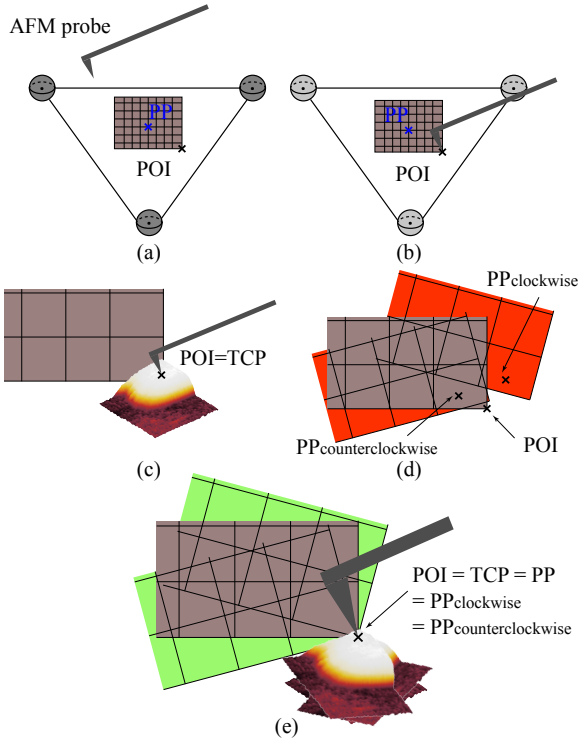

Fig. 2: Main steps for the in-plane center of rotation identification and control. (a) Initial position of the AFM probe. (b) Probe landing at the vicinity of the POI. (c) AFM topography imaging. (d-e) Clockwise and counterclockwise rotations of the sample holder around the POI with the kinematic method (d) and the SEM refining method (e).

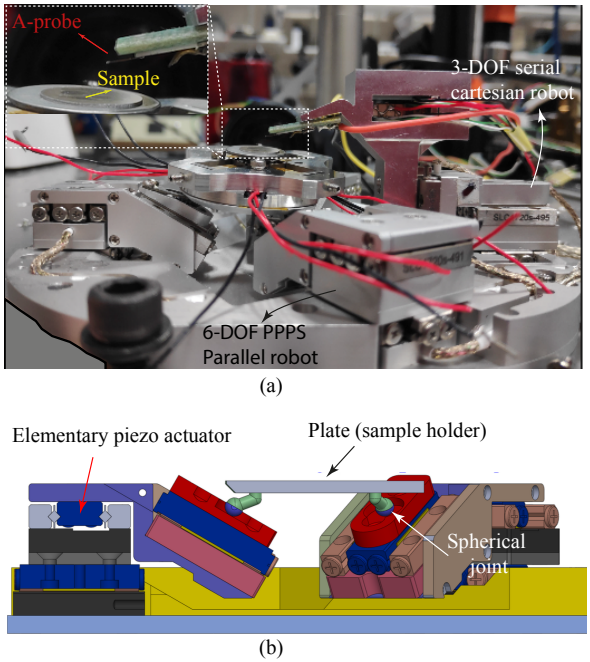

Fig. 3: (a) Micro-robotic platform. (b) Side view of the CAD model of the parallel robot.

dimensional space with reduced friction. These backlashes introduce uncertainties in the relative position and rotation within the joints and, consequently, lead to a loss of accuracy of the end effector or platform [16]–[20].

The objective of this letter is to propose a method to identify and control the in-plane center of rotations of parallel micro-robotic structures so that any micrometer-scale sample observed with a SEM can be rotated around the tip of an AFM with micrometer precision. The robotic structure consists of a parallel platform with spherical joints (Fig. 1) serving as a sample holder and a Cartesian structure allowing the AFM probe to move [12], [14]. The question raised in this letter is related to a kinematic robotic calibration problem, but it has specific challenges because of the required accuracy needed for the robot to operate at the microscale. Firstly, the clearances in the spherical joints are of the same order of magnitude as the robot's required accuracy. For instance, a spherical joint with 3 mm in diameter can produce a 4 μm clearance [20]. Secondly, the correction of the errors by vision feedback requires a high magnification microscope. In this study, the micro-robotic system operates inside an electron microscope, enabling the observation of objects on a scale of less than 1 μm. Thirdly, the method proposed in this letter requires the use of a micrometer sized end effector, e.g. AFM cantilever for a high precision estimation of a point of interest (POI). The particularity of the proposed method is that it is well suited to deal with calibration issues of high precision robotic systems operating at the micrometer scale.

The letter is structured as follows: section II presents the main issues of the work and an overview of the methods. Section III describes the experimental equipment used for the study. A detailed description of the methods and the robotic strategies with experimental results are presented in sections IV and V. Section VI shows the effectiveness of the method when using non-calibrated samples. Section VII summarizes the work and concludes the letter.

II. Objectives and Methods

The objective is to control the rotations of the sample holder around a point of interest (POI). The main steps of the method are illustrated in Fig. 2. SEM images are used to define the POI and to guide the AFM probe for a landing at the vicinity of the POI (Fig. 2 (a) and Fig. 2 (b)). An AFM topography imaging is performed for a precise positioning of the probe on the POI (Fig. 2 (c)). The goal is co-locate the Pivot Point (PP) of the parallel robot with the POI. To identify the coordinate of the POI in the frame of reference of the sample holder, a kinematic Tool Center Point (TCP) calculation is performed. The calculation of the TCP is based on the hand-eye method for robotic systems [21]–[23] and is adapted for the specific case of the study. This approach is called in this letter the "kinematic method". The PP being sensitive to the spherical joint backlash [20], its coordinates are different when performing clockwise ($PP_{clockwise}$) and counterclockwise rotations ($PP_{counterclockwise}$) as illustrated in Fig. 2 (d). Therefore, the aforementioned method is completed using SEM images data so that true PP coincides with POI for in-plane rotations (Fig. 2 (e)). This approach is referred as "SEM refining method".

III. Experimental Imaging Platform

It is composed of a Scanning Electron Microscope (SEM) in which an AFM system operates. The latter is controlled with home made algorithms implemented in a MicroLabBox (dSPACE) unit. The AFM is composed of a 3-DOF Cartesian robot and a 6-DOF PPPS parallel platform (Fig. 3 (a)). The side view of the CAD model of the parallel robot is shown in Fig. 3 (b). The Cartesian robot holds an Akiyama AFM probe (A-probe). The A-probe operates on the principle of self-sensing using a quartz piezoelectric tuning fork [14], [24].

The sample holder is a PPPS parallel robot, composed of (Fig. 1) three pairs of identical active prismatic joints A_1 and A_2 in series, followed by a passive prismatic joint A_3 and a passive spherical joint S that is attached to the main sample holder platform. It can be operated by defining poses with respect to its base frame. The main objective of the parallel robot is to ensure an in-plane displacement and an in-plane rotation of the sample. This micro-robotic AFM system has been characterized, modeled and controlled in previous works [12], [20], [25], [26]. More specifically, in [20], the model of the PPPS kinematic chain includes the non-linearities of the spherical joints. The objective has been to analyse the effect of joints clearances on the positioning accuracy of the micro-robotic system. Considering spherical joints with 3 mm in diameter with a clearance of 4 μm, a clearance contact stiffness of 10^6 N/m and a contact damping of 10^6 N.s/m, it has been shown that positioning errors of the parallel robot in the order of the μm occurs. This is in accordance with experimental observations. This work has demonstrated that in the whole kinematic chain of the robot, the spherical joints play a predominant role in the positioning error.

Existing AFM in SEM platforms [5]–[8] have translational axes without the ability to rotate the AFM probe relatively to the sample. However, there exist AFM robotic systems (not inside SEM) with one out of plane rotational dof that allow probe rotation or sample holder rotation [10]. The AFM system proposed in the letter is the unique one with the ability to provide both in plane and out of plane rotations of the probe relatively to the sample. The main sample used for this study is a TipsNano TGX1 calibration grating consisting of a square pattern with 3 µm period in which each square is 1.6 µm in length. The imaging conditions of the SEM used during the experiments are: 20 kV of beam voltage potential, 300 nA of sample current and 1.7 A of filament current. These conditions are kept constant for all measurements.

IV. In-Plane Center of Rotation Determination using Kinematic Method and AFM Data

The kinematic method is based on the classical hand-eye problem of industrial robotics in which the transformation between a flange frame F of a robot (default controlled frame) and the frame of the tool fixed on the flange (Tool Center Point or TCP) is unknown. A classical way to solve this problem is to bring the tool to a fixed known position using different robot configurations [21], [22]. Given that, for each configuration, the position of the TCP must be the same and the TCP transformation must be constant for all configurations.

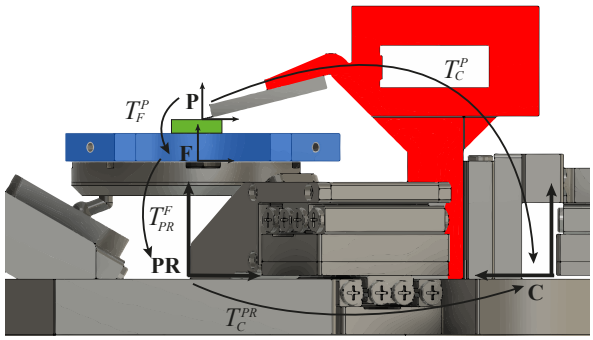

Fig. 4: CAD view of the robotic structure with its main frames and their transformations.

Each pair of configurations yields a system of linear equations that can be solved to determine the TCP with respect to the flange [23]. In this letter, the method is adapted considering the particular case of a closed kinematic chain, i.e the AFM tip brings into contact the Cartesian and the parallel structures. The sample is placed on top of the plate of the parallel robot which is equivalent to its robot flange. Hence, the task of rotation control is equivalent to identify how the POI is positioned with respect to the flange frame and to place the TCP of the parallel robot at this position.

A. Reference frames and transformations

The reference frames of interest are (Fig.4):
- Frame C: the base frame of the 3-DOF Cartesian robot.
- Frame PR: the base frame of the parallel robotic platform where the sample is fixed.
- Frame F: the "flange" frame of the parallel robotic platform located at the center of the plate. This is the default TCP of the robot. The XY plane of F is ideally co-planar with the parallel robot plate.
- Frame P: the frame located at the point of contact between the AFM probe tip and the sample surface. The origin of this frame is the POI.

When the AFM probe tip is in contact with a POI, the following matrix equation must be respected.

$$T_C^P = T_C^{PR} T_{PR}^F T_F^P \tag{1}$$

where the T are 4×4 transformation matrices in a homogeneous space containing 3×3 rotation matrices R and 3×1 translation vectors $\vec{t}$.

$$T = \begin{bmatrix} R_{3\times3} & \vec{t}_{3\times1} \\ \hat{0}_{1\times3} & 1 \end{bmatrix} \tag{2}$$

Each of these transformations can be described as follows:
- T_C^{PR}: is fixed and depends on the assembly of robot.
- T_{PR}^F: is the transformation from PR to F which is accessible from any position.
- T_F^P: is the transformation from F to P. This is the unknown to be determined. In this study, the orientation of this frame R_F^P is defined as the unit matrix $\mathbb{1}_{3\times3}$.
- T_C^P: is the transformation between C and the POI. In this study, the matrix R_C^P is the same as R_C^F, given that $R_F^P = \mathbb{1}_{3\times3}$.

The unknown $T_F^P = X$ is set as:

$$X = \begin{bmatrix} \mathbb{1}_{3\times3} & \vec{t}_X \\ \hat{0}_{1\times3} & 1 \end{bmatrix} \tag{3}$$

where $\vec{t}_X = [x_{tcp}, y_{tcp}, z_{tcp}]^T$ contains the coordinates of the desired TCP and must coincide with the POI and the point of contact with the AFM probe.

B. Calculation of the coordinates of the TCP

There are an infinite number of configurations of the parallel and the Cartesian robots for which the AFM probe touches a POI. Let i and j be two of these configurations. Considering (1), i and j must respect:

$$T_{C(i)}^P = T_C^{PR} T_{PR(i)}^F X \quad \text{and} \quad T_{C(j)}^P = T_C^{PR} T_{PR(j)}^F X \tag{4}$$

By subtracting both equations and multiplying both sides of the resulting expression by T_{PR}^C, one can obtain:

$$T_{PR}^C \left(T_{C(i)}^P - T_{C(j)}^P \right) = \left(T_{PR(i)}^F - T_{PR(j)}^F \right) X \tag{5}$$

By expanding (5) into their rotational and translational components, it is possible to obtain a matrix equation. Taking the translational part of the previous expression leads to:

$$R_{PR}^C \left(\vec{t}_{C(i)}^P - \vec{t}_{C(j)}^P \right) = \left(R_{PR(i)}^F - R_{PR(j)}^F \right) \vec{t}_X + \vec{t}_{PR(i)}^F - \vec{t}_{PR(j)}^F \tag{6}$$

This expression can be rearranged as a system of linear equations with $\vec{t}_X$ the unknown vector:

$$D_{PR(ij)}^F \vec{t}_X = \vec{b}_{ij} \tag{7}$$

where:

$$D_{PR(ij)}^F = R_{PR(i)}^F - R_{PR(j)}^F \tag{8}$$

$$\vec{b}_{ij} = R_{PR}^C \left(\vec{t}_{C(i)}^P - \vec{t}_{C(j)}^P \right) - \left(\vec{t}_{PR(i)}^F - \vec{t}_{PR(j)}^F \right) \tag{9}$$

This expression is similar to the one in [23], except for the term $R_{PR}^C \left(\vec{t}_{C(i)}^P - \vec{t}_{C(j)}^P \right)$. This system can be extended to deal with the measurement noise. For this, one can construct an over-defined system of linear equations in which every set of two configurations adds three more equations to the system. In the case of four different configurations numbered by the indexes $i = \{1,2,3,4\}$, it is possible to find $\vec{t}_X$ by solving the following system of non-redundant 18 equations:

$$\begin{bmatrix} D_{PR(12)}^F \\ D_{PR(13)}^F \\ \vdots \\ D_{PR(34)}^F \end{bmatrix} \vec{t}_X = \begin{bmatrix} \vec{b}_{12} \\ \vec{b}_{13} \\ \vdots \\ \vec{b}_{34} \end{bmatrix} \tag{10}$$

Equation (10) can be solved using Ordinary Least Squares (OLS). All the lines in the matrices $D_{PR(ij)}^F$ must be non-zero and linearly independent from each other. A practical way to achieve this is by ensuring that all the rotations θ_x, θ_y and θ_z of the parallel robot are different for each configuration.

Equation (9) shows that all translations appear as relative positions, this means that the method does not need absolute positions neither from the parallel nor from the Cartesian robot. However, the translations of the Cartesian robot are multiplied by R_{PR}^C. Hence, any inaccuracy in this matrix will be amplified by the length $\left(\vec{t}_{C(i)}^P - \vec{t}_{C(j)}^P \right)$. The accuracy of R_{PR}^C depends on how well known is the orientation of the base frame of the parallel robot with respect to that of the Cartesian robot. This will be added to whatever previous inaccuracies were already in $\vec{t}_{C(i)}^P$ caused by the geometrical model of the Cartesian robot, e.g. due to a poor orthogonality of the axes. Hence, if there are inaccuracies in the Cartesian robot, we recommend to move it as little as possible between configurations in order to avoid this problem.

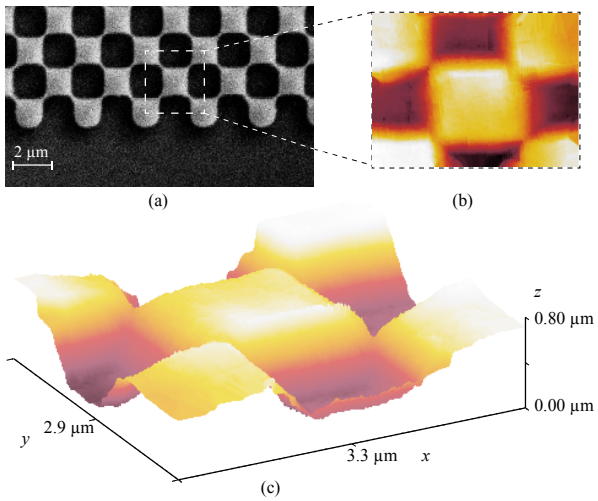

Fig. 5: Images of the TGX1 calibration grid observed with the SEM (a) and the AFM (b)(c).

In a more general sense, the most ideal type of configuration consists of small translations for the Cartesian robot and the parallel robot, while having orientations different enough to guarantee a maximum rank for the matrices $D_{PR(ij)}^F$. Because of this, it is recommended to place the TCP in a position known to be in the vicinity of the POI to avoid large translational movements. This also means that the method can be performed in an iterative way, so a first gross estimation can be refined by a second round of the method. This second round can use configurations obtained after having rotated around the TCP calculated in the previous iteration.

C. Determination of the coordinates of the point of interest using AFM

The images of the SEM are used to define a POI. The feature chosen is a corner of the calibration grating TGX1 (Fig.5). For the first iteration, the set of the four configurations of the parallel robot are defined using the flange frame F as the TCP. The values of the rotation angles are shown in Table I. For each set of angles, the parallel robot is moved to approach the tip of the AFM to the furthermost square of the calibration grid's corner. Once this is done, the coordinates of $\vec{t}_{PR(i)}^F$ can be defined. Now that the AFM probe is in the vicinity of the region of interest, its tip is landed on the sample. An AFM scan is then performed in order to precisely identify the position of the square's corner, that is $\vec{t}_{C(i)}^P$. An example of an AFM image of the TGX1 taken with the system is shown in Fig.5

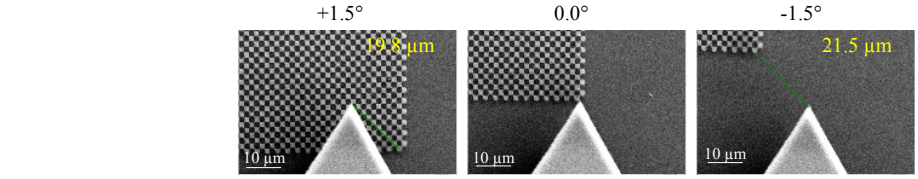

(a) Estimation of the TCP with the CAD model

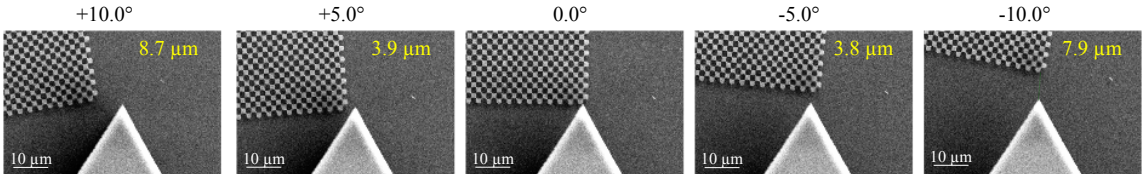

(b) Estimation of the TCP with the Kinematic method (Iteration 2)

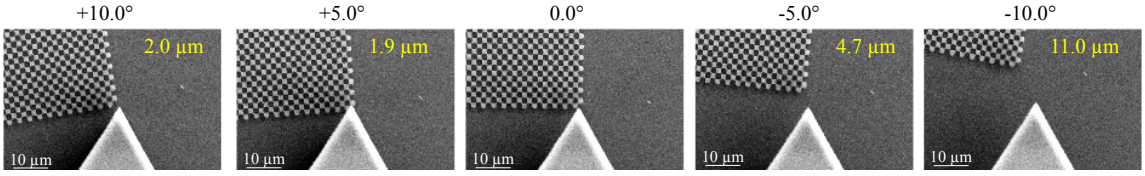

(c) Counterclockwise pivot refinement

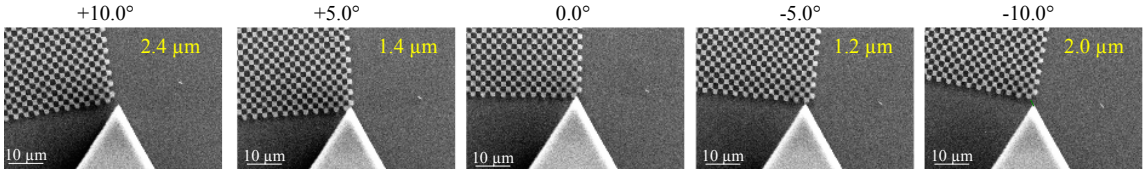

(d) Clockwise and Counterclockwise pivot refinement

Fig. 6: SEM images showing the rotations of the sample holder around the Z-axis: (a) ±1.5° rotation with the TCP estimated using the CAD model. (b) ±10.0° rotation with the TCP calculated in the second iteration of the kinematic method. (c) ±10.0° rotation with the counterclockwise pivot refinement using SEM vision. (d) ±10.0° rotation with the clockwise and counterclockwise pivot refinements using SEM vision. The yellow numbers indicate the distance between the POI and the probe.

TABLE I: Rotation angles used for four different parallel robot configurations.

Configuration index	θ_x	θ_y	θ_z
1	0°	0°	0°
2	2°	2°	2°
3	−3°	−3°	−3°
4	3°	−2°	5°

(b) and Fig.5 (c). This procedure is repeated for all angle configurations. Once all the data is gathered, it is possible to define the linear system of equations (10).

Table II shows the resulting TCP coordinates calculated for two iterations of the kinematic method. These results are compared with the coordinates of the TCP estimated considering the dimensions of the TGX 1 calibration grating, its position on the sample holder and the ideal CAD (Computer-Aided Design) model of the parallel robot. In iteration 1, the mean value of the norm of the residuals is 56.22 μm. In iteration 2, this mean value drops down to 13.18 μm. That means that, in iteration 2, the solutions of equation (10) for the calculation of the coordinates the TCP are closer to each others within the tens of μm. If more iterations are done, no significant improvement in the result is observed. The systematic errors of the geometrical model, the calibration errors, backlash or a combination of all are such that the method does not allow to determine the coordinates of the TCP beyond this level of accuracy. Fig.6 (a) and Fig.6 (b) show the results of a rotation θ_z of ±1.5° and ±10.0° around the TCP whose coordinates are calculated respectively with the CAD model and the kinematic method with two iterations. With the TCP estimated by the CAD model, it is enough for the robotic platform to rotate 1.5° around the Z axis for the POI to move 22.9 µm away from the AFM probe. For a ±5.0° rotation using the CAD model, the calibrated grid will be outside the SEM field of view. This is why it is not shown in Fig.6 (a). When the TCP is calculated with the kinematic method, the pivot point is much closer to the POI. With a 5° rotation clockwise and counterclockwise, the POI is distant from the AFM probe by 3.8 µm and 3.9 µm respectively.

V. In-Plane Center of Rotation Determination using SEM Refining Method

Thanks to kinematic method with AFM, the true pivot point is in the SEM image field of view when using a 4800 × magnification. Thus, this method is a good way to establish adequate initial conditions for the SEM refinement method. The latter is based on the measurement, with the SEM vision,

TABLE II: TCP coordinates obtained with the kinematic method and estimated with the CAD model.

Coordinates	CAD model	Kinematic method (Iteration 1)	Kinematic method (Iteration 2)
x_{tcp}	$-1500.00\,\mu$m	$-1503.44\,\mu$m	$-1010.67\,\mu$m
y_{tcp}	$1500.00\,\mu$m	$1969.30\,\mu$m	$2114.96\,\mu$m
z_{tcp}	$14\,000.00\,\mu$m	$13\,364.96\,\mu$m	$13\,574.90\,\mu$m

of the positions of reference structures (Fig. 7) during the in-plane rotation of the robotic platform. These measurements allow the determination of the real position of the pivot point in the image plane and its distance from the POI. Therefore, the position of the pivot point in the X and Y axes can be corrected. The following calculations are performed under the assumption that the surface of the calibration grating is parallel to the SEM projection plane. This assumption is not completely true but is sufficient to ensure that the estimate of the pivot point coordinates is accurate to within a few μm.

A. Estimation of the parallel robot base frame

The objective is to define a reference frame on the SEM image aligned with the base frame of the parallel robot. The pixel values are transformed into distances by using the default scale of the image. An initial image reference frame I is defined as being aligned with the pixel lines and rows. To deduce the direction of the base frame, parallel robot movements are made along the X and Y axes and the coordinates of the reference structures (red squares in Fig. 7) are measured for three positions along the same axis. Between two images k and l, the most accurate solution for the translation vector (by OLS) is the mean vector of the displacement of all individual points. That is, if the positions of each point in a given image k is defined by the coordinates $\vec{p}_n^{\,k} = [x_n^k, y_n^k]$ with $n = \{1, 2, \dots, N\}$, then the closest translation from image k to image l called $\vec{m}^{kl}$ is:

$$\vec{m}^{kl} = \frac{1}{N} \sum_{n=1}^{N} \left(\vec{p}_n^{\,l} - \vec{p}_n^{\,k} \right) \tag{11}$$

To determine the vector that best fits the displacement between three or more images, it is possible to do the following. Let us define $\vec{m}^{kl} = \left[m_x^{kl}, m_y^{kl} \right]^T = s^{kl} [1 \;\; u]^T$, where s^{kl} and u are scalars. The orientation of the vector $\vec{m}^{kl}$ is completely defined by the value of u, while s^{kl} contains the scaling factor and the direction of the vector. Also, $[1 \;\; u]^T$ is not a unitary vector. These definitions lead to the expression:

$$m_x^{kl} u = m_y^{kl} \tag{12}$$

Given that all the movements are done along the same direction, this is true for any pair of images kl. Hence, for three images, the following over defined system of linear equations can be defined:

$$\begin{bmatrix} m_x^{12} & m_x^{13} & m_x^{23} \end{bmatrix}^T u = \begin{bmatrix} m_y^{12} & m_y^{13} & m_y^{23} \end{bmatrix}^T \tag{13}$$

This can be solved using Total Least Squares (TLS).

Once the value of u is determined, the unitary vector $\vec{n}_x$ or $\vec{n}_y$ can be determined dividing $[1 \;\; u]^T$ by its norm. A rotation matrix $R = [\vec{n}_x \;, \vec{n}_y]^T$ can be used to transform all points of the image frame I into the base frame R of the parallel robot.

B. Rotation around a pivot different from the origin

Let's take a set of points $\vec{p}_i$ that must rotate around the point $\vec{c}$ using a pure rotation with the rotation matrix R. The following approach can be used: i) Subtract the coordinates of $\vec{c}$ from all points $\vec{p}_i$. ii) Multiply the result with the matrix R. iii) Add $\vec{c}$ to recenter the points around the true origin. The result is the following operation:

$$\vec{p}_i^{\,r} = R\,(\vec{p}_i - \vec{c}) + \vec{c} \tag{14}$$

$\vec{p}_i^{\,r}$ are the points after the rotation around $\vec{c}$, from the same frame of reference as the one used for $\vec{p}_i$. Equation (14) looks like to the general equation (15) for a rigid transformation of a set of points with known correspondences.

$$\vec{p}_i^{\,r} = R\vec{p}_i + \vec{t} \tag{15}$$

The rotation performed by R is done around the origin of the reference frame and the translation performed by $\vec{t}$ is measured in this same reference frame. In the form of equation (15), the problem of rigid transformations of point clouds is well known in the literature. As explained in [27], [28], the way to solve them is by using Singular Value Decomposition (SVD) to perform a Least Squares minimization of the expression:

$$(R, \vec{t}) = argmin \sum_{i=1}^{N} \| R\vec{p}_i + \vec{t} - \vec{p}_i^{\,r} \|^2 \tag{16}$$

R is the same rotation matrix in both expressions (14) and (15). On the other hand, the position of the pure rotation pivot $\vec{c}$ can be written as follows:

$$\vec{c} = (\mathbb{1}_{2\times 2} - R)\vec{t} \tag{17}$$

$\mathbb{1}_{2\times 2}$ is a 2×2 unitary matrix. Based on this, what follows is to find the parameters R and $\vec{t}$ through the SVD method [27], [28] and to use equation (17) to calculate the pivot point $\vec{c}$. For this calculation, a set of 12 points that include the POI ($\vec{p}_O$) will be used, as shown in Fig.7.

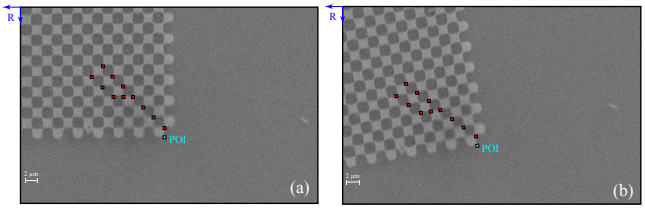

Fig. 7: SEM images with a) zero rotation around Z-axis and b) +9° rotation around Z-axis. The TCP used is that identified with the kinematic calculation of section IV.

C. Estimation of R, $\vec{t}$ and $\vec{c}$ using SVD

The 12 points are subjected to an unknown in-plane rotation around an unknown pivot. This is a special case in 2D of the generalised rigid transformation problem of equation (15). To find the arguments of equation (16), the following procedure can be used [27]: i) Calculate respectively the mean vectors $\vec{m}$ and $\vec{m}^r$ of the points $\vec{p}_i$ and $\vec{p}_i^r$ before and after rotation:

$$\vec{m} = \frac{1}{N}\sum_{i=1}^{N}\vec{p}_i \quad \wedge \quad \vec{m}^r = \frac{1}{N}\sum_{i=1}^{N}\vec{p}_i^r \tag{18}$$

ii) Calculate the covariance matrix H by summing the outer products of each corresponding pair of points minus their respective means:

$$H = \sum_{i=1}^{N}(\vec{p}_i - \vec{m})(\vec{p}_i^r - \vec{m}^r)^T \tag{19}$$

In this case, H is a 2×2 matrix. iii) Perform a SVD on the matrix H so that $H = USV^T$. With this, calculate the rotation matrix R and the translation vector $\vec{t}$:

$$R = VU^T \quad \wedge \quad \vec{t} = \vec{m}^r - R\vec{m} \tag{20}$$

Now that R and $\vec{t}$ are found, the pivot point $\vec{c}$ can be calculated using equation (17). Finally, to obtain the correction of the TCP previously calculated with the kinematic method, it is possible to take the values of the coordinates of the POI ($\vec{p}_O$) from the SEM image before rotation and subtract the value of $\vec{c}$. The result is then added to the TCP of the robot's geometric model. Thanks to this, it is possible to calculate the coordinates of as many center of rotations as wanted relying on the TCP calculation of only one pivot point.

D. Results and discussions

The pivot point is not constant during a rotation. It changes position according to the direction of rotation. The most likely hypothesis for this phenomenon lies in the very nature of spherical joints and the mechanical clearances they generate. Thus, during calculation, the coordinates of the pivot points $PP_{clockwise}$ and $PP_{counterclockwise}$, corresponding respectively to clockwise and anti-clockwise rotation (see Fig.2), are identified. Whatever the direction of rotation, the method enables the robot's TCP to be placed on the POI with micrometric precision. Fig.6(c) shows results when only the counterclockwise pivot point is calculated and is used for both direction of rotation. It can be seen that when rotating clockwise, the distance between the POI and the AFM probe is much larger than with counterclockwise rotation. When calculating both the $PP_{clockwise}$ and $PP_{counterclockwise}$ and taking the adequate one for each rotation, the maximum distance between the AFM probe and the POI is 2.4 μm for a 10 ° rotation as shown in Fig.6(d).

Table III shows the coordinates of the TCP obtained with the kinematic method and the SEM refining method. The accuracy obtained by combining the kinematic method and the SEM refinement method is sufficient when the AFM probe operates within a range of a few tens of micrometers. The proposed method brings a new feature to SEM technology: an AFM can be used to identify the TCP related to any point of interest around which the sample has to be rotated, enabling observation of the latter from different viewing angles. This can reveal structures that can only be observed after rotation around a specific point of interest.

TABLE III: TCP coordinates obtained with the kinematic method and the SEM refining method (clockwise and counterclockwise).

Coordinates	Kinematic method (Iteration 2)	SEM refining method (counter-clockwise)	SEM refining method (clockwise)
x_{tcp}	−1010.67 µm	−1018.52 µm	−977.13 µm
y_{tcp}	2114.96 µm	2076.29 µm	2115.22 µm

VI. In-plane rotation of a random sample around a point of interest using AFM in SEM

A sample containing spheres a few tens of micrometers in diameter is inserted into the SEM. The user first selects as many POIs as desired from the SEM computer screen. Here, three POIs are selected (Fig. 8 (a)). The aim is to perform rotations in the plane of the sample holder around the points of interest. To achieve this, the AFM probe is brought into contact with the sample at POI 1 to perform the TCP calculation. The kinematic method and the SEM refining method are used to deal with POI 1. As all the three POIs are in the filed of view of the microscope, the TCP of POI 1 and the SEM refining method are used to deal with POI 2 and POI 3. Fig. 8 (b), Fig. 8 (c) and Fig. 8 (d) show the superposition of three SEM images as the sample holder rotates around the tip of the AFM probe at POI 1, POI 2 and POI 3 respectively. Fig. 9 shows a side view of Fig. 8 (b) with the AFM tip. A video is linked to the letter to highlight the results of the study.

VII. Conclusion

This letter has shown how an AFM system can be used in synergy with a SEM to locate, identify and control the center of rotation of a sample holder around any POI in the accessible

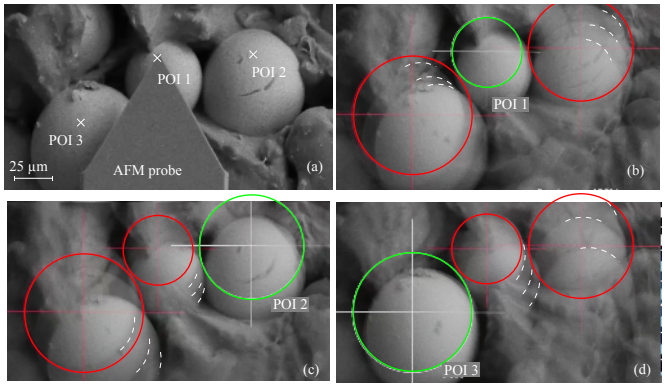

Fig. 8: SEM view with selected POIs (a). Rotation around POI 1 (b), POI 2 (c) and POI 3 (d). The dotted arcs highlight the contour of the sample spheres for each angle of rotation.

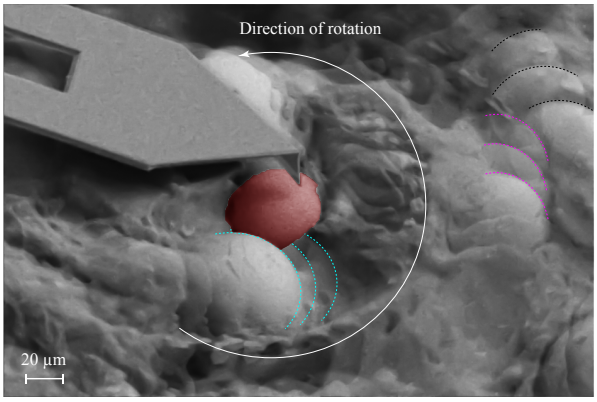

Fig. 9: Superposition of three SEM images as the sample holder rotates around the tip of the AFM probe at POI 1. The dotted arcs highlight the contour of the sample spheres for each angle of rotation. Only the sphere at POI 1 (highlighted by a false color) is almost at the same position when rotation occurs.

AFM workspace. Although only in-plane rotations are taken into account in the final result, out-of-plane rotations of the sample holder were necessary for the TCP calculations. This required a parallel 6 DOF robot to move the sample holder. Spherical joints are one of the best solutions for achieving in-plane and out-of-plane rotations, but they are characterized by an inherent backlash that introduces uncertainties in the position of the center of rotation. The methods proposed in this letter enable in-plane rotation of the sample holder around the AFM tip with micrometer precision despite the spherical joint backlash. If the joints were perfect, the kinematic method and AFM data would be enough to obtain the desired results. The SEM refinement method is an efficient complement to deal with the joints imperfections. Rotations capabilities demonstrated in this letter are of importance for several applications involving AFM such as manipulation, characterization and topography imaging at the small scales. The proposed method also shows a new functionality for correlative AFM in SEM.

ACKNOWLEDGMENT

This work has been sponsored by the ANR project Robine (ANR-19-CE33-0005) and Robotex 2.0.

REFERENCES

[1] Hui Xie and Stéphane Régnier. High-efficiency automated nanomanipulation with parallel imaging/manipulation force microscopy. *IEEE Transactions on Nanotechnology*, 11:21–33, 2012.

[2] E Usukura, A Narita, A Yagi, S Ito, and J Usukura. An unroofing method to observe the cytoskeleton directly at molecular resolution using atomic force microscopy. *Nature Scientific Report*, 6:27472, 2016.

[3] Hans-Jurgen Butt, Brunero Cappella, and Michael Kappl. Force measurements with the atomic force microscope: Technique, interpretation and applications. *Surface Science Reports*, 59:1–152, 2005.

[4] G R. Heath, E Kots, J L. Robertson, S Lansky, G Khelashvili, H Weinstein, and S Scheuring. Localization atomic force microscopy. *Nature*, 594:385–390, 2021.

[5] M. Winhold, M. Leitner, P. Frank, N. Hosseini, J. Sattelkov, G.E. Fantner, H. Plank, and C.H. Schwalb. Correlative in-situ analysis on the nanoscale by combination of afm and sem. *Microscopy and Microanalysis*, 24(S1):1922–1923, 2018.

[6] M Holz, C Reuter, A Ahmad, A Reum, M Hofmann, T Ivanov, and I W. Rangelow. Correlative microscopy and nanofabrication with afm integrated with sem. *Microscopy Today*, 27(6):24–30, 2019.

[7] V Novotna, J Horak, M Konecny, V Hegrova, O Novotny, Z Novacek, and J Neuman. Afm-in-sem as a tool for comprehensive sample surface analysis. *Microscopy Today*, 28(3):38–46, 2020.

[8] Stephan Kleindiek, Massoud Dadras, Klaus Schock, Andreas Lieb, and Gregor Renka. *Combining SEM with AFM for in situ Correlative Microscopy*, pages 999–1000. John Wiley & Sons, Ltd, 2016.

[9] Hui Xie, Danish Hussain, Feng Yang, and Lining Sun. Development of three-dimensional atomic force microscope for sidewall structures imaging with controllable scanning density. *IEEE/ASME Transactions on Mechatronics*, 21(1):316–328, 2016.

[10] Danish Hussain, Khurshid Ahmad, Jianmin Song, and Hui Xie. Advances in the atomic force microscopy for critical dimension metrology. *Measurement Science and Technology*, 28(1):012001, 2016.

[11] Y Liu, J Deng, and Q Su. Review on multi-degree-of-freedom piezoelectric motion stage. *IEEE Access*, 6:59986–60004, 2018.

[12] M Boudaoud, T Lu, S Liang, R Oubellil, and S Régnier. A voltage/frequency modeling for a multi-dofs serial nanorobotic system based on piezoelectric inertial actuators. *IEEE/ASME Transactions on Mechatronics*, 23(6):2814–2824, 2018.

[13] W Dong, D Rostoucher, and M Gauthier. Kinematics parameters estimation for an afm/robot integrated micro-force measurement system. In *International Conference on Intelligent Robots and Systems*, 2010.

[14] Freddy Romero Leiro, Stéphane Régnier, and Mokrane Boudaoud. Correction of angular deviations in AFM samples from generic topographic data. In IEEE Robotics and Automation Society, editors, *IEEE/RSJ International Conference on Intelligent Robots and Systems*, Kyoto, Japan, 2022.

[15] Haojian Lu, Wanfeng Shang, Hui Xie, and Yajing Shen. Ultrahigh-precision rotational positioning under a microscope: Nanorobotic system, modeling, control, and applications. *IEEE Transactions on Robotics*, 34(2):497–507, 2018.

[16] Jokin Aginaga, Oscar Altuzarra, Erik Macho, and Xabier Iriarte. Assessing position error due to clearances and deformations of links in parallel manipulators. *Journal of Mechanical Design*, 135:1–8, 2013.

[17] Xin Li, Xilun Ding, and Gregory Chirikjian. Analysis of angular-error uncertainty in planar multiple-loop structures with joint clearances. *Mechanism and Machine Theory*, 91:69–85, 2015.

[18] Jianhong Hou, Guofeng Yao, and Huili Huang. Dynamic analysis of a spatial mechanism including frictionless spherical clearance joint with flexible socket. *Journal of Computational and Nonlinear Dynamics*, 13:1–12, 2017.

[19] Selçuk Erkaya. Effects of joint clearance on motion accuracy of robotic manipulators. *Strojniški vestnik - Journal of Mechanical Engineering*, 64:82–94, 2017.

[20] Michael Pumphrey, Mahmoud Al-Tamimi, Aylar Abouzarkhanifard, Mohammad Al Janaideh, Stéphane Régnier, and Mokrane Boudaoud. Analysis of the effect of clearance in spherical joints on the rotation accuracy of parallel type micro-robotic systems. In *IEEE/RSJ International Conference on Intelligent Robots and Systems*, pages 8551–8556, Prague, Czech Republic, 2021.

[21] Y.C. Shiu and S. Ahmad. Calibration of wrist-mounted robotic sensors by solving homogeneous transform equations of the form ax=xb. *IEEE Transactions on Robotics and Automation*, 5(1):16–29, 1989.

[22] Klaus H. Strobl and Gerd Hirzinger. Optimal hand-eye calibration. In *IEEE/RSJ International Conference on Intelligent Robots and Systems*, pages 4647–4653, Beijing, China, 2006.

[23] Johan Hallenberg. Robot tool center point calibration using computer vision. Dissertation, Institutionen for systemteknik, 2007.

[24] T Akiyama, N F. de Rooij, U Staufer, M Detterbeck, D Braendlin, S Waldmeier, and M Scheidiger. Implementation and characterization of a quartz tuning fork based probe consisted of discrete resonators for dynamic mode atomic force microscopy. *Review of Scientific Instruments*, 81(6):063706, 2010.

[25] Ali Bazaei, Mokrane Boudaoud, Massoud Hemmasian Ettefagh, Zhiyong Chen, and Stéphane Régnier. Displacement sensing by piezoelectric transducers in high-speed lateral nanopositioning. *IEEE Sensors Journal*, 19(20):9156–9165, 2019.

[26] Raouia Oubellil, Alina Voda, Mokrane Boudaoud, and Stéphane Régnier. Robust control strategies of stick-slip type actuators for fast and accurate nanopositioning operations in scanning mode. In *Mediterranean Conference on Control and Automation (MED)*, 2015.

[27] Olga Sorkine-Hornung and Michael Rabinovich. Least-squares rigid motion using svd, 2016. Technical note.

[28] K. S. Arun, T. S. Huang, and S. D. Blostein. Least-squares fitting of two 3-d point sets. *IEEE Transactions on Pattern Analysis and Machine Intelligence*, PAMI-9(5):698–700, 1987.